

Hydrodynamic instability of shells accelerated by direct ion beam heating

M. M. Basko^{a)} and J. A. Maruhn

Institut für Theoretische Physik, Universität Frankfurt, P.O. Box 11 19 32, Robert-Mayer-Str. 8-10, D-60054 Frankfurt, Germany

T. Schlegel

TU Darmstadt, Institut für Kernphysik, Schloßgartenstr. 9, D-64289 Darmstadt, Germany

(Received 25 July 2001; accepted 28 January 2002)

The Rayleigh–Taylor (RT) instability of planar shells accelerated by direct heating of an underlying absorber layer is analyzed. A specific feature of the problem considered is a fixed in space energy deposition region, which allows the unstable transition layer to develop only gradually as the heated matter is pushed out of the deposition region. The linear growth spectrum $\omega(k)$ is investigated by relating a simple analytic estimate for a stationary exponential transition layer with the results of two-dimensional hydrodynamic simulations. For the unperturbed motion, an analytic solution is used which describes a uniform acceleration of the payload driven by a time-dependent uniform heating of the absorber with a fixed spatial extension. It is shown that an enhancement factor of $1.5(h/d)$, where h is the effective half-thickness of the heated region and d is the in-flight thickness of the payload, can be achieved for the distance-moved-over-thickness ratio as compared to the classical RT case of a strong density jump. © 2002 American Institute of Physics.

[DOI: 10.1063/1.1462634]

I. INTRODUCTION

When intense beams of heavy ions are discussed as a driver option for inertial confinement fusion (ICF) targets, it is usually in the context of indirect drive: On target, the ion beam energy is first converted into thermal x-rays, which then drive the implosion of a spherical deuterium–tritium fuel shell.^{1,2} Very little attention has been given so far to direct acceleration of fluid shells by the ion beam heating. The main obstacle for direct shell acceleration is associated with nonuniformities of the beam energy deposition (especially, in the case of several overlapping beams), and with the Rayleigh–Taylor (RT) instability in the vicinity of the payload–absorber interface. In this paper we address the problem of the hydrodynamic instability in the situation when a low-entropy shell (payload) is accelerated by thermal pressure generated in the adjacent absorber layer, which is heated by an intense beam of ions (or any other source of volumetric heating with controlled spatial distribution and temporal history). Although more important for practical applications would probably be the case of spherical or cylindrical shells, in the present work we restrict our treatment to the simplest case of planar geometry. The ion beam heating is modeled as a prescribed source of specific energy deposition $q(t, x, y)$ [ergs $\text{g}^{-1} \text{s}^{-1}$].

The main disadvantage of the direct drive by ion beams—as compared with the ablative drive by laser or x-ray irradiation—is the absence of the ablative stabilization. The reason is that the ions heat up the entire absorber mass from the onset of the irradiation pulse, and both the heat conduction and the mass flow across the unstable interface

are typically insignificant. Our goal in this work was to find out to what extent the RT instability can be stabilized by a finite density gradient, and what conditions should be satisfied in order to achieve maximum stabilization in the case of direct ion illumination. Our statement of the problem corresponds to a tangential (with respect to the unstable interface) irradiation pattern, which appears to be better suited for suppressing the RT instability than the commonly assumed case of normal ion incidence, and which, to the best of our knowledge, has not been discussed in literature so far.

As was shown in numerous studies,^{3–5} the linear growth rate ω of critical RT instability modes in the case of ablative shell acceleration is reduced by a significant factor ≥ 2 with respect to the classical value $\omega_{\text{RT}} = (gk)^{1/2}$ (here g is the shell acceleration, k is the wave number of the instability mode). As a consequence, ablatively driven shells can be accelerated over distances $s \geq (30–40)d$ (d is the in-flight thickness of the shell)—which is crucial for the success of ICF.¹

When the absorber layer is directly heated by an ion beam and a density jump, $\rho_p > \rho_a$, occurs between the payload and the absorber, the payload–absorber interface is subject to the classical RT instability. Even with infinitely small initial perturbations, a mixing layer develops along the unstable interface, which advances into the heavy fluid in a self-similar fashion as

$$h_{\text{mix}}(t) = \alpha_b A g t^2, \quad (1)$$

where $A = (\rho_p - \rho_a) / (\rho_p + \rho_a)$ is the Atwood number, $\alpha_b = 0.04–0.05$ for the two-dimensional (2D) motion, and $\alpha_b = 0.06–0.07$ for the 3D motion.^{6–8} As a consequence, an accelerated shell with $A \approx 1$ is broken by the instability at a time when $h_{\text{mix}}(t) \approx d$, i.e., at a time by which the distance-moved-over-thickness ratio $\text{DMOT} \equiv s/d = \frac{1}{2} g t^2 / d \approx (2\alpha_b)^{-1} = 7–10$. It is basically these fundamental facts

^{a)}On leave from: Institute for Theoretical and Experimental Physics, Moscow, Russian Federation. Electronic mail: m.basko@gsi.de

which led to rather pessimistic conclusions about the prospects of direct-drive heavy ion ICF targets.⁹ These targets, however, have been analyzed under the assumption of normal (radial) incidence of the irradiating ion beams. Since the range of fast ions is, to a first approximation, nearly constant in mass coordinate, the beam absorption front travels with matter and tends to create a sharp unstable density gradient near the absorber–payload interface.

A qualitatively different situation arises when the fast ions propagate parallel to the absorber–payload interface, and the payload is accelerated from a uniform state without initial density contrast. Such an irradiation geometry can be envisaged for acceleration of planar shells and in cylindrical implosions. In this case the energy deposition region, being confined to the beam aperture, remains fixed in space, and the unstable layer develops only gradually, as the absorber material expands beyond the beam aperture. The scale height of the unstable layer can be quite different from that under the normal incidence and, as a consequence, one can expect significantly higher DMOT values. Our analysis, based on simple analytical models and 2D numerical simulations, indicates an enhancement factor of $\approx 1.5(h/d)$ for the DMOT, where h is an effective half-thickness of the heating region (typically associated with the focal spot radius of the irradiating ion beam).

Besides possible ICF applications, this work has been motivated also by recent progress in concentrating the energy deposition by heavy ion beams in matter. Energy deposition levels of up to 1–3 kJ/g have already been achieved at the Gesellschaft für Schwerionenforschung (GSI, Darmstadt), and a beam induced hydrodynamic motion has been directly observed.^{10,11} Significantly higher deposition values in the range of 10–100 kJ/g are expected from the near-future facilities at GSI (SIS-100)¹² and at the Institute for Theoretical and Experimental Physics in Moscow.¹³ The envisaged beam parameters are well suited for hydrodynamic experiments in the cylindrical geometry, and, in particular, for cylindrical implosions of thin cold shells accelerated by thermal pressure in the beam heated absorber layer.^{14,15} In such experiments the RT instability may be one of the key factors limiting maximum achievable values of the radial convergence ratio.

II. UNPERTURBED MOTION

To describe the unperturbed motion, we construct a simple analytic solution of the 1D hydrodynamic equations, which reproduces the main features of shell acceleration by direct energy deposition in a fixed region of space. We assume that the unperturbed flow is along the y axis, assign the $y=0$ value to the motionless center of mass of a planar slab, and consider only the region $y>0$. In addition, we assume that the beam heating occurs so that there is no mass transfer across the $y=0$ plane, i.e., that the pressure peak occurs in the center of mass of the slab and the flow velocity $u(t, y=0)=0$ for all $t>0$.

A general assumption that we make about the spatial distribution of the heating rate $q(t, y)$ is that the heating zone is fixed in space, i.e., confined to a fixed interval $0<y<h$ in

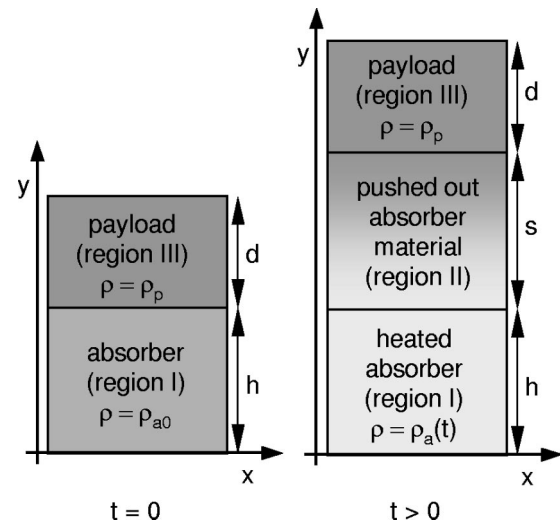


FIG. 1. A planar payload shell (region III) is accelerated by thermal pressure generated by heating the absorber material in region I. The lower boundary $y=0$ is assumed to be a motionless plane of symmetry.

the $y>0$ half-space. Then, an effective half-thickness h of the heated region can be referred to as the beam focal radius, whenever the ion trajectories lie in the (x, z) -plane perpendicular to the direction of shell acceleration. Such a configuration may, for example, be considered as a planar approximation to the cylindrical implosion of a thin cold liner driven by a hollow (or a rapidly rotating) beam of fast ions propagating along the axis of a cylindrical target.¹⁵

Initially, as it is shown in Fig. 1, our configuration consists of two uniform layers: The absorber (region I) at $0<y<h$ with a density ρ_{a0} , and the payload (region III) at $h<y<h+d$ with a density ρ_p . Later on, as region I gets heated, part of the absorber material is pushed out beyond the $y=h$ plane and forms an expanding region II at $h<y<h+s$ between the accelerated payload (now at $h+s<y<h+s+d$) and the heated part of the absorber. The solution that we seek should describe a uniform acceleration of the payload with $s=\frac{1}{2}gt^2$, where g is a constant acceleration.

To obtain an analytic solution, we use the ideal-gas equation of state

$$\epsilon = \frac{1}{\gamma - 1} \frac{P}{\rho}, \tag{2}$$

and write down the 1D hydrodynamic equations in the Lagrangian form

$$\frac{\partial y}{\partial t} = u, \tag{3}$$

$$\frac{\partial u}{\partial t} + \frac{\partial P}{\partial m} = 0, \tag{4}$$

$$\frac{\partial \epsilon}{\partial t} + P \frac{\partial u}{\partial m} = q(t, m) \tag{5}$$

with respect to the mass coordinate

$$m = \int_0^y \rho(t, y') dy', \tag{6}$$

$$0 \leq m \leq m_a + m_p, \quad m_a = \rho_{a0}h, \quad m_p = \rho_p d. \quad (7)$$

For a constant acceleration g of the payload, the solution to Eqs. (3)–(5) is quite simple in the nonheated regions II and III (at $y > h$), namely, all the thermodynamic quantities are functions of m only, with

$$P(t, m) = P(m) = g(m_a + m_p - m), \quad (8)$$

and the velocity $u(t, m) = gt$ is independent of m . The density profile $\rho(t, m) = \rho(m)$ in region II is found by matching the solutions in regions I and II.

The solution in region I is constructed by assuming the simplest kinematically consistent velocity profile

$$u(t, y) = \begin{cases} gt \frac{y}{h}, & 0 < y < h \\ gt, & h < y < h + s + d \end{cases}, \quad (9)$$

and by calculating the functions $\rho(t, m)$, $P(t, m)$, and $q(t, m)$ from Eqs. (3)–(5). Having integrated Eq. (3), we find

$$y(t, m) = \begin{cases} \frac{m}{\rho_{a0}} \Lambda(t), & 0 < m < m_a \Lambda^{-1} \\ h \left(1 + \ln \frac{m}{m_a} \right) + \frac{1}{2} g t^2, & m_a \Lambda^{-1} < m < m_a, \\ h + \frac{m - m_a}{\rho_p} + \frac{1}{2} g t^2, & m_a < m < m_a + m_p \end{cases} \quad (10)$$

where

$$\Lambda = \Lambda(t) = \exp\left(\frac{gt^2}{2h}\right). \quad (11)$$

The density profile is given by

$$\rho(t, m) = \left(\frac{\partial y}{\partial m}\right)^{-1} = \begin{cases} \rho_{a0} \Lambda^{-1}(t), & 0 < m < m_a \Lambda^{-1} \\ \frac{m}{h}, & m_a \Lambda^{-1} < m < m_a \\ \rho_p, & m_a < m < m_a + m_p \end{cases}. \quad (12)$$

From Eq. (4) we calculate the pressure profile in region I

$$P(t, m) = g \left[m_p + m_a + \frac{m_a}{2\Lambda} \left(\frac{gt^2}{h} - 1 \right) \right] - \frac{m^2 g}{2m_a} \left(1 + \frac{gt^2}{h} \right) \Lambda, \quad (13)$$

and from Eq. (5) we find the heating rate in the same region

$$q(t, m) = q_0(t) - \left(\frac{m}{m_a} \Lambda\right)^2 q_1(t) = q_0(t) - \left(\frac{y}{h}\right)^2 q_1(t), \quad (14)$$

where

$$q_0(t) = \frac{g^2 t}{\gamma - 1} \left[\gamma \left(1 + \frac{m_p}{m_a} \right) \Lambda + (\gamma - 1) \frac{gt^2}{2h} + \frac{3 - \gamma}{2} \right], \quad (15)$$

$$q_1(t) = \frac{g^2 t}{\gamma - 1} \left[(\gamma + 1) \frac{gt^2}{2h} + \frac{3 + \gamma}{2} \right]. \quad (16)$$

Thus obtained heating rate has a simple inverted parabolic profile in space, which resembles realistic particle current

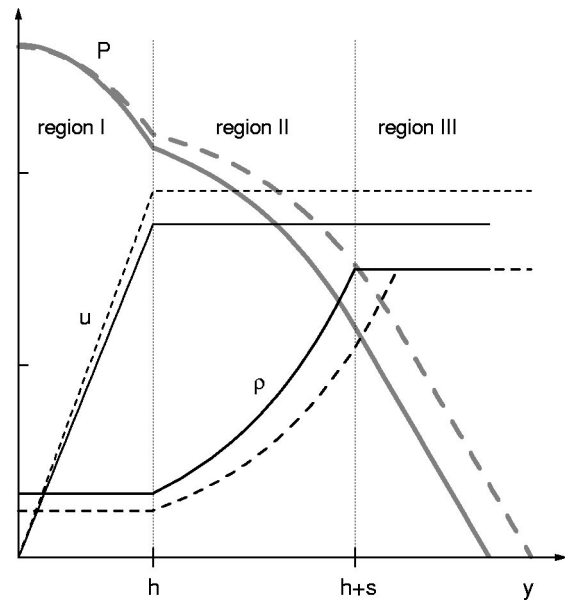


FIG. 2. Pressure, density, and velocity profiles in the unperturbed solution at two neighboring times t (solid curves) and $t + \Delta t$ (dashed curves).

distributions in ion beams. A strong (exponential) dependence of q_0 on time is stipulated by the necessity to maintain a constant acceleration of the payload.

The spatial profiles of $u(t, y)$, $\rho(t, y)$, and $P(t, y)$, as given by Eqs. (8)–(13), are shown in Fig. 2 for two neighboring times t and $t + \Delta t$. The key features of the density profile, important for subsequent instability analysis, are that (i) the density of the accelerated payload, $\rho = \rho_p$, remains constant in space and time, and (ii) the density in region II below the payload increases exponentially

$$\rho(t, y) = \rho_a(t) \exp\left(\frac{y}{h} - 1\right), \quad (17)$$

from the value

$$\rho_a(t) = \rho(t, h) = \rho_{a0} \exp\left(-\frac{gt^2}{2h}\right), \quad (18)$$

at $y = h$ to ρ_{a0} at $y = h + s = h + \frac{1}{2} g t^2$. If $\rho_{a0} = \rho_p$ (the case of main interest here), the density is a continuous function of y . The pressure profile $P(t, y)$ is an inverted parabola in region I, and a combination of the exponential and linear functions in regions II and III.

In our solution, the heating rate $q(t, y)$ has its minimum at $y = h$, and this minimum value can become negative within a certain time interval for certain combinations of γ , m_a , and m_p . For $\gamma < 2$ one can avoid negative heating rates by satisfying the condition

$$\frac{m_a}{m_p} \leq \frac{\gamma}{2 \exp(\gamma/2 - 1) - \gamma}. \quad (19)$$

When $\gamma \geq 2$, the heating rate (14)–(16) is non-negative for any $m_a, m_p \geq 0$. For $\gamma = 5/3$ one needs $m_a/m_p \leq 63.38$; when $m_a/m_p \leq 4.693$, condition (19) is fulfilled for any $\gamma \geq 1$.

III. ANALYTIC EVALUATION OF THE LINEAR GROWTH RATE

In our unperturbed solution, region II is clearly Rayleigh–Taylor unstable.^{16,17} If not stated to the contrary, we always assume $\rho_{a0} = \rho_p$, i.e., a continuous density profile, which develops from an initially uniform configuration and for which one would expect a maximum stabilizing effect due to the finite density gradient. Then, the structure of the unperturbed flow shown in Fig. 2 resembles closely a transition layer with the exponential density profile analyzed by Mikaelian.¹⁸ However, because the thickness of the transition layer, $s = \frac{1}{2}gt^2$, varies essentially in time, it would be absolutely unwarranted to try to reach quantitative conclusions by applying solely the Mikaelian’s model. Hence, we use the Mikaelian’s solution mainly as a reference formula, which helps us to interpret the quantitative results obtained from the 2D numerical simulations.

Following Mikaelian, we evaluate the linear growth rate ω of a small perturbation with a wave number k

$$\delta\rho(t,x,y) = \delta\rho(y) \exp(ikx + \omega t), \quad (20)$$

by assuming that (i) the fluid is incompressible, (ii) regions I and III are half-spaces extending, respectively, to $y = -\infty$ and $y = +\infty$, whereas the thickness s of region II is fixed, and (iii) all the three regions I–III have the same acceleration g in the $+y$ direction. Then (for details see Refs. 17 and 18)

$$\omega^2 = \frac{g/h}{1 + (2kh)^{-2} \mp (\chi/ks)^2}, \quad (21)$$

where $\chi = \chi(kh, s/h)$ is the solution of the transcendental equation

$$\chi \coth(\chi) + \frac{\chi^2}{2ks} = \frac{s}{2h} \left(\frac{1}{4kh} - kh \right), \quad (22)$$

for the long-wavelength branch

$$0 < kh < \left(\frac{1}{4} + \frac{h^2}{s^2} \right)^{1/2} - \frac{h}{s} \quad (23)$$

[– sign in Eq. (21)], or of the equation

$$\chi \cot(\chi) - \frac{\chi^2}{2ks} = \frac{s}{2h} \left(\frac{1}{4kh} - kh \right), \quad (24)$$

for the short-wavelength branch

$$\left(\frac{1}{4} + \frac{h^2}{s^2} \right)^{1/2} - \frac{h}{s} < kh < \infty, \quad (25)$$

[+ sign in Eq. (21)]. Note that there is only one solution $0 < \chi < \infty$ to Eq. (22) in the long-wavelength branch, and an infinite discrete series $0 < \chi_1 < \chi_2 < \dots$ ($\omega_1 > \omega_2 > \dots$) of solutions to Eq. (24) in the short-wavelength branch. We are interested in the fastest growing mode $\omega = \omega_1$, which corresponds to $0 < \chi = \chi_1 < \pi$ in Eq. (24). In the limit of $s \gg h$, Eqs. (21)–(25) reduce to a simple formula

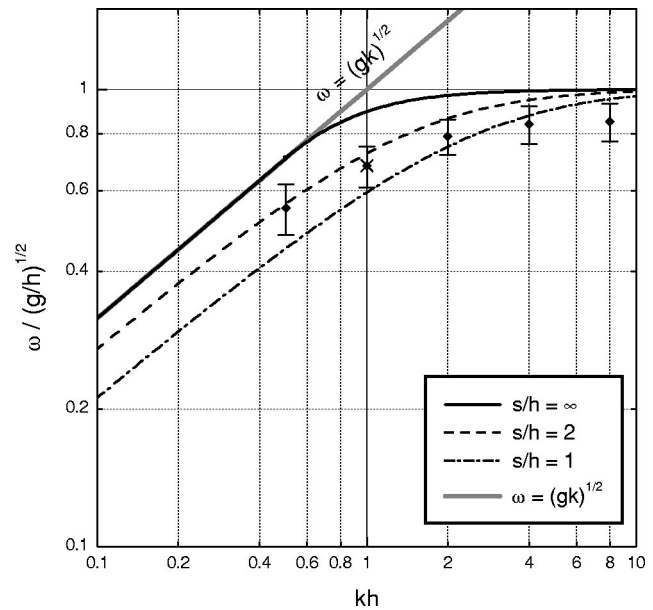


FIG. 3. Linear growth rate [normalized to $(g/h)^{1/2}$] as a function of the dimensionless wave number kh . Results of 2D simulations for $h=1$ (5 black diamond points with “uncertainty” bars) and $h=2$ (an x cross point for $kh=1$) are compared with the analytic formulas (21)–(26) plotted for three different values of the ratio s/h .

$$\omega^2 \equiv \omega_h^2 = \begin{cases} gk, & 0 < kh < \frac{1}{2} \\ \frac{g/h}{1 + (2kh)^{-2}}, & \frac{1}{2} < kh \end{cases}. \quad (26)$$

Figure 3 shows the plots of $\omega/(g/h)^{1/2}$ as a function of kh calculated from Eqs. (21)–(25) for three different values of the ratio s/h . As one would expect, the growth rate saturates at $\omega = (g/h)^{1/2}$ in the short-wavelength limit $kh \gg 1$ for any value of s/h , and approaches the classical RT value $\omega = (Agk)^{1/2}$ [with $A = (\rho_p - \rho_a)/(\rho_p + \rho_a) = \tanh(s/2h)$] for long wavelengths $kh \ll 1$.

IV. RESULTS OF 2D NUMERICAL SIMULATIONS

To verify how realistic values of the linear growth rate ω compare with the analytic estimates of the previous section, we have conducted a series of 2D hydrodynamic simulations. There are several reasons to suspect that the growth rates observed under realistic conditions may differ significantly from simple estimates (21)–(26).

First of all, because the thickness of the transition layer $s = \frac{1}{2}gt^2$ depends on time, the growth rate of a given mode k also becomes time dependent. Since $\omega = \omega(kh, s/h)$ increases with s for given k and h , one would expect the limiting formula (26) to give an upper bound for realistic growth rates. Another reason for effective reduction of the ω values observed over a finite period of time is the infinite number of solutions to Eq. (24) (for fixed k , h , and s) with progressively decreasing values of ω_n : An arbitrary initial perturbation with a wave number k will generally relax to a superposition of modes with successively decreasing values of ω_n rather than just to the fastest growing mode ω_1 plotted in Fig. 3.

Also, the finite thickness d of the accelerated shell [not accounted for in Eqs. (21)–(26)] has a stabilizing effect for long ($kd < 1$) wavelengths.¹⁹

The effect of compressibility, on the contrary, is expected to increase the value of ω . When applied to the exponential density profile $\rho(y) \propto e^{y/h}$, the growth rate calculated by Bandiera²⁰ for a compressible fluid in the short-wavelength limit $kh \gg 1$ becomes

$$\omega = \left[\frac{g}{h} \left(1 + \frac{gh}{c^2} \right) \right]^{1/2}, \tag{27}$$

where $c = (\gamma P/\rho)^{1/2}$ is the local sound speed. This “compressible” value of ω is always larger than the corresponding incompressible limit of $\omega = (g/h)^{1/2}$, but the enhancement factor $(1 + gh/c^2)^{1/2}$ rapidly approaches 1 as one moves away from the payload–absorber interface into the heated region.

The 2D simulations discussed below have been done with the Lagrangian–Eulerian hydrodynamics code CAVEAT, based on a Godunov-type numerical scheme for a quadrangular mesh.²¹ The code has no heat conduction, and we have augmented it only with appropriate energy deposition and data analysis routines. The simulated region was chosen exactly as shown in Fig. 1, with x values spanning the interval $0 < x < L$. The three boundaries $x=0$, $x=L$, and $y=0$ were treated as frictionless rigid walls (reflective boundary conditions), whereas the upper $y=h+s+d$ boundary was set to be a free Lagrangian surface at zero pressure. The initial unperturbed state was assigned according to the solution of Sec. II at $t=0$. A constant acceleration of the payload was ensured by prescribing the heating law (14)–(16). When not stated to the contrary, the adiabatic index $\gamma=2$ was used.

A. Classical case of a density jump

First we consider the case with a density jump $\rho_p : \rho_{a0} = 10:1$ ($\rho_p = 1$, $\rho_{a0} = 0.1$) across the payload-absorber interface. Here we expect the 2D code to reproduce the classical result $\omega_{RT} = (Agk)^{1/2}$ for a single instability mode k —at least for sufficiently large $k \gg h^{-1}$, when the exponential density profile in region II has a negligible influence on modes localized near the unstable interface. A corresponding divergence-free initial perturbation was introduced for the velocity field only,

$$\delta u_y(t=0, x, y) = a_0 \cos(kx) \exp(-k|y-h|), \tag{28}$$

$$\delta u_x(t=0, x, y) = a_0 \text{sign}(y-h) \sin(kx) \exp(-k|y-h|). \tag{29}$$

To evaluate the growth rate of a given mode k , we analyze the temporal behavior of the Fourier amplitudes

$$a_y(t) = \frac{\int_0^L [y_{fc}(t, x) - \bar{y}_{fc}(t)] \cos(kx) dx}{\int_0^L \cos^2(kx) dx}, \tag{30}$$

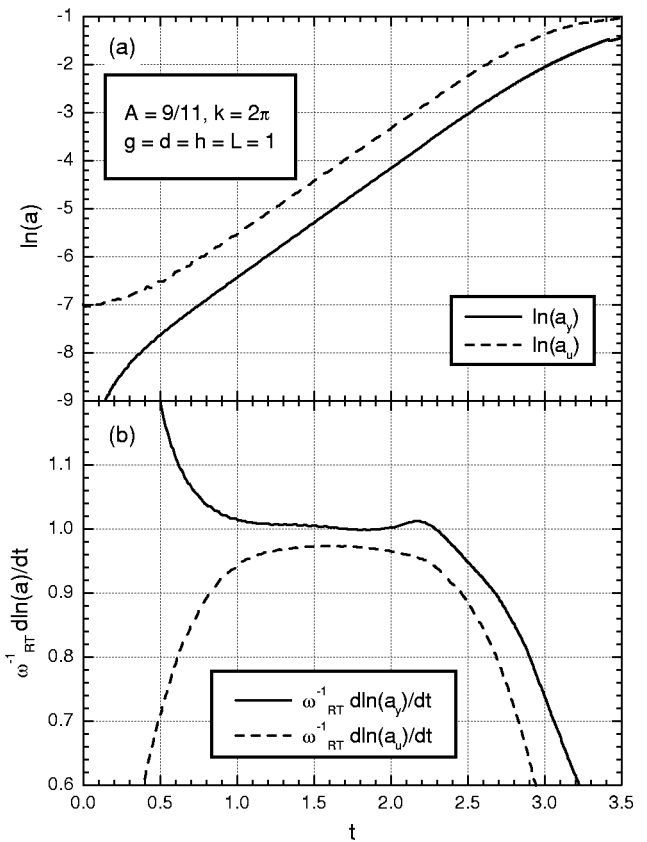


FIG. 4. Growth rate of a perturbation mode $k=2\pi$ for a density jump $\rho_p : \rho_{a0} = 10:1$ as inferred from the 2D CAVEAT simulation with 40 mesh zones per wavelength. (a) Temporal evolution of $\ln(a_y)$ and $\ln(a_u)$, where the Fourier amplitudes $a_{y,u}$ are defined in Eqs. (30) and (31). (b) Linear growth rate $\omega = d \ln(a_{y,u})/dt$ normalized to the classical RT value $\omega_{RT} = (Agk)^{1/2} = 2.2673$.

$$a_u(t) = \frac{\int_0^L [u_{y,fc}(t, x) - \bar{u}_{y,fc}] \cos(kx) dx}{\int_0^L \cos^2(kx) dx}, \tag{31}$$

of the perturbations in the vertical position $y_{fc}(t, x)$ of the unstable interface, and in the y velocity component $u_{y,fc}(t, x)$ of this interface. Because the integrals in Eqs. (30) and (31) are evaluated numerically, it is important to subtract from $y_{fc}(t, x)$, $u_{y,fc}(t, x)$ the mean values

$$\bar{y}_{fc}(t) = \frac{1}{L} \int_0^L y_{fc}(t, x) dx, \tag{32}$$

$$\bar{u}_{y,fc}(t) = \frac{1}{L} \int_0^L u_{y,fc}(t, x) dx. \tag{33}$$

Numerical identification of the unstable interface between regions II and III and determination of $y_{fc}(t, x)$ and $u_{y,fc}(t, x)$ is trivial for purely Lagrangian simulations, but requires a special criterion in the mixed Lagrangian–Eulerian mode.

Figures 4 and 5 show the results of simulations for the case of $L=h=d=1$, $g=1$, $k=2\pi$ (one wave period over $0 < x < L$), $a_0 = 10^{-3}$ on a 40×90 mesh [a 80×160 mesh in

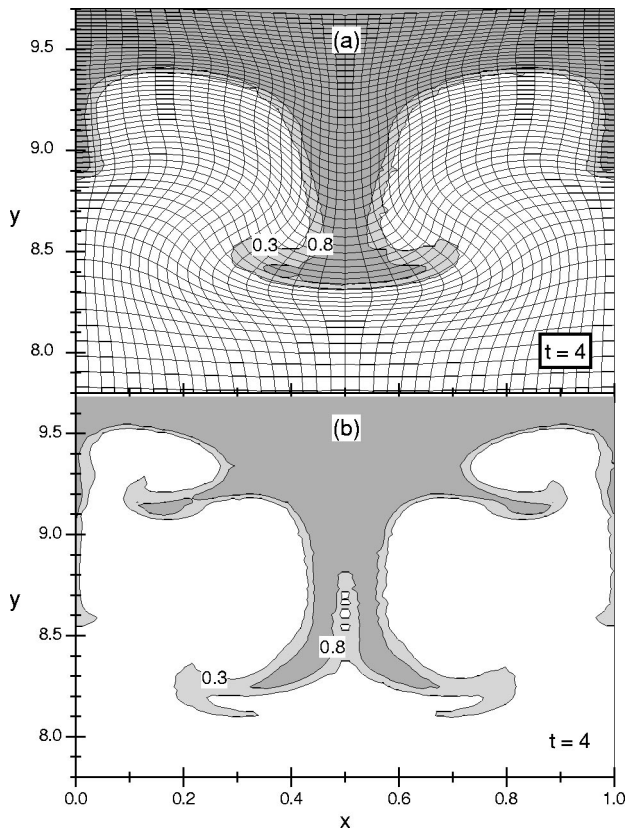


FIG. 5. Density contours in the vicinity of the unstable interface at $t=4$ for the case of a 10:1 density jump as calculated with (a) 40 and (b) 80 mesh zones per wavelength; in case (a) the mesh is also plotted.

Fig. 5(b)]. The simulations have been performed in the mixed Lagrangian–Eulerian mode with the value of ALECOEF=0.99, i.e., close to a purely Lagrangian mode, and with the advection remapping at every 100th Lagrangian time step (NADVSKP=100). For the data analysis, the position of the unstable interface, $y = y_{fc}(t, x)$, was identified as a density contour $\rho = 0.5\rho_p$. Figure 4(a) clearly demonstrates that, after an initial relaxation period of $t \leq 0.5-1.0$, the logarithms of the perturbation amplitudes $a_y(t)$, $a_u(t)$ grow linearly with time until the exponential growth begins to saturate at $t > 2.5$. The linear growth rate inferred from Fig. 4(b) agrees well [within $\pm 1\%$ for $a_y(t)$] with the classical RT value of $\omega_{RT} = (Agk)^{1/2} = 2.2673$. The results for 80 mesh zones per wavelength look practically identical.

Figure 5 shows the structure of the instability mode at $t=4$ (9.06 e -foldings after the start of simulation), when the evolution is already in the nonlinear stage. It was possible to reach this stage only in the Lagrangian–Eulerian mode: Due to large mesh distortions, a pure Lagrangian run (with $a_0 = 10^{-3}$) can hardly get beyond $t=3$ and demonstrates a 3% lower growth rate ω . An apparent feature of the displayed structure is the presence of higher harmonics. As we double the number of mesh points per wavelength [compare Fig. 5(b) with Fig. 5(a)], the number of short-scale details also doubles. A combination of two factors appears to give rise to these short-scale features, namely, (i) the fact that our initial perturbation is not exactly an eigenmode for a given k , and (ii) the increase of the growth rate, $\omega \propto k^{1/2}$, with the wave

number k . A closer scrutiny reveals that higher harmonics with wave numbers $2k, 3k, \dots$ appear already during the initial relaxation period at $t \leq 0.5-1$ on a level of $\leq 2\%$ with respect to the principal mode k (presumably, mainly as a consequence of finite differencing). Having faster growth rates, they catch up with the principal mode after some 5–8 e -folding times for the latter. Note that the numerical algorithm of the CAVEAT code is stable in the sense that no visible perturbations evolve along the unstable interface by $t=4$ when we start with $a_0=0$.

B. Continuous density variation

For a continuous density profile we cannot even try to make the initial perturbation close to the instability eigenmode simply because the thickness of the transition layer, $s = \frac{1}{2}gt^2$, rapidly evolves in time, and eigenmodes in the usual sense do not exist. By analogy with the previous case—although somewhat arbitrary—we introduce a divergence-free velocity perturbation

$$\delta u_y(t=0, x, y) = a_0 \cos(kx) \exp[-k^2(y-h)^2], \tag{34}$$

$$\delta u_x(t=0, x, y) = 2a_0k(y-h) \sin(kx) \exp[-k^2(y-h)^2], \tag{35}$$

on the premise that our goal is to explore the evolution of small perturbations on a characteristic scale k^{-1} localized near the unstable interface between regions II and III. The functional form of the y -dependence in Eqs. (34) and (35) is chosen such that (i) the perturbation decays exponentially away from $y=h$ on a length scale k^{-1} , and (ii) the perturbed velocity field is continuous—which must be the case for a continuous density distribution.

We have performed a series of simulations for different values of k and h , all starting with $a_0 = 10^{-3}$ and all having $\rho_p = \rho_{a0} = 1$, $g = 1$, $d = 1$ (by fixing g and d , we actually choose convenient time and length units). In all cases only one wave period along x was simulated, i.e., L was set equal to $2\pi/k$.

Figures 6 and 7 present detailed information on instability growth for the case of $k = 2\pi$ ($L = 1$), $h = 1$. Similar to the classical case of a density jump, the perturbation growth in Fig. 6(a) follows closely a straight line of exponential amplification, $a_{y,u} \propto e^{\omega t}$, after a short ($t \leq 1$) period of initial relaxation. However, the growth rate $\omega = d \ln(a_{y,u})/dt$, plotted in Fig. 6(b), is not quite constant: It increases noticeably from $\omega \approx 0.77$ at $t \approx 2.5$ to $\omega \approx 0.88-0.93$ at $t \approx 6$. Such an increase cannot be explained by variation of the transition layer width $s = \frac{1}{2}gt^2$ simply because the perturbation scale $k^{-1} = (2\pi)^{-1}$ is much shorter than the value of s at $t \geq 2$. We have verified it by performing a separate run for a slab with a fixed value of $s = 1$, accelerated by a boundary pressure applied from below to region I. The resulting values of $d \ln(a_{y,u})/dt$, plotted in Fig. 6(b) as thick gray curves, practically coincide with those in the heating case with $s = \frac{1}{2}gt^2$. The latter implies that the observed ω variation is caused by special properties of the eigenmode spectrum in exponential transition layers,¹⁸ i.e., by the presence of an infinite series of eigenmodes for a given (not too small) k with successively

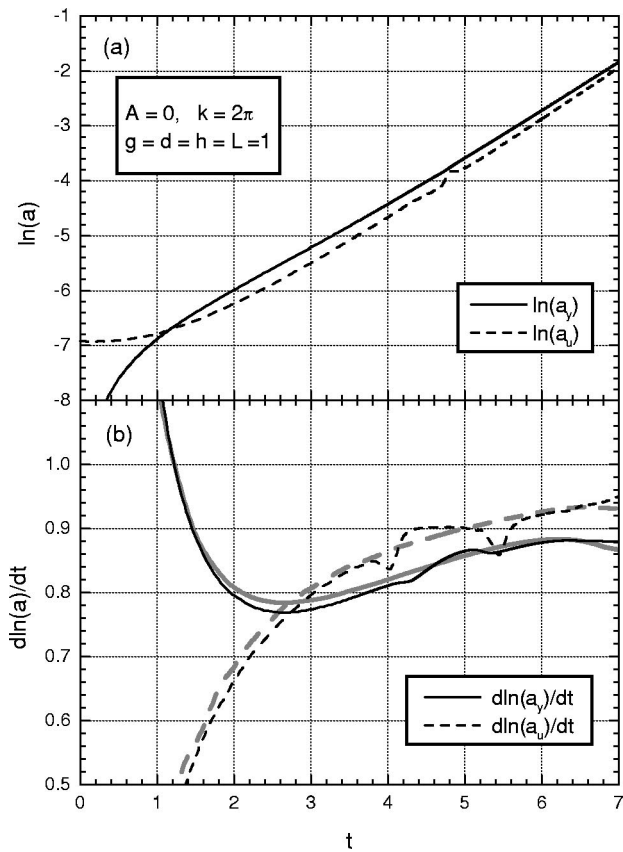


FIG. 6. Same as Fig. 4 but for a continuous ($\rho_{a0} = \rho_p$) density variation. (b) Thick gray curves show the growth rates obtained in a 2D simulation of an exponential transition layer with a fixed thickness $s = 1$.

decreasing values of ω_n . Initially, our perturbation relaxes to a certain superposition of such modes, and only then the fastest growing mode ω_1 gradually wins over the others. In Fig. 3, the “uncertainty” bars for numerically calculated values of $\omega(k)$ indicate the range of this variation observed over 4 to 5 e -folding times.

Figure 7 shows the structure of the $k = 2\pi$ mode observed in two different simulations, namely, (a) in a pure Lagrangian run with 40 mesh zones per wavelength until $t = 7$, and (b) in a Lagrangian–Eulerian run with 80 mesh zones per wavelength until $t = 8$. In distinction from Fig. 5, no traces of higher harmonics are noticeable. This is a clear manifestation of the fact that for a continuous density variation on a height scale h the growth rate of short-wavelength modes, $kh \gg 1$, saturates at $\omega \approx (g/h)^{1/2}$ independent of the k value.¹⁶ Even though the higher modes do appear during the initial relaxation period, having no advantage in the growth rate, they never catch up with the principal mode. This circumstance, combined with the absence of tangential discontinuities in the perturbed velocity field, reduces Lagrangian mesh deformations and allows us to use purely Lagrangian simulations for evaluation of the linear growth rates. In addition, identification of the unstable interface becomes more difficult and much more noisy in the Lagrangian–Eulerian simulations of continuous density profiles. Note that the Lagrangian simulation of Fig. 7(a) could not be pursued beyond $t = 7$ because of the mesh deformation not near the unstable

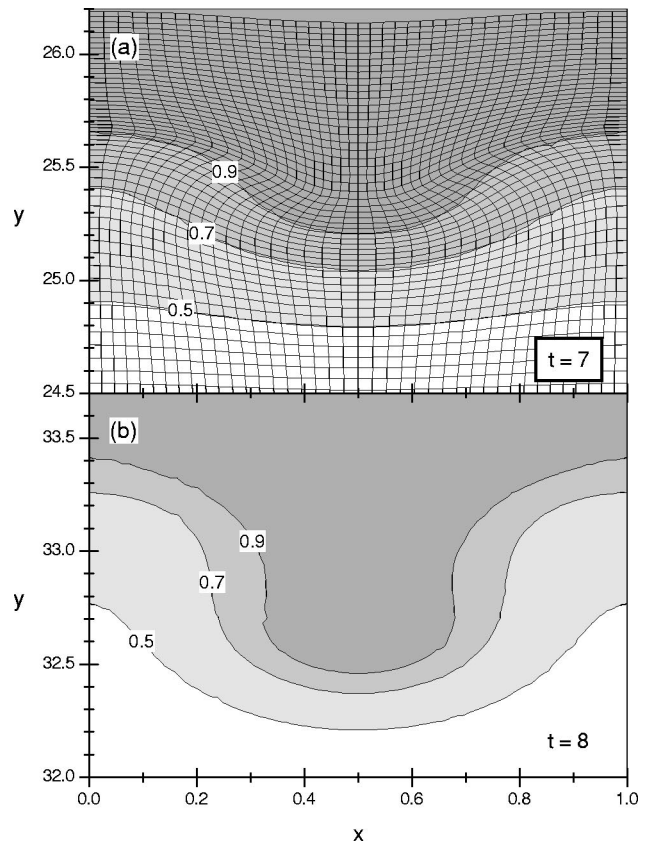


FIG. 7. Same as Fig. 5 but for a continuous ($\rho_{a0} = \rho_p$) density variation and at different times (a) $t = 7$ and (b) $t = 8$.

interface but at the upper free fluid boundary [not shown in Fig. 7(a)], where a cusp-like structure develops.

In Fig. 3, the calculated values of the growth rate, $\omega(k)$, are given for five different values of k with corresponding uncertainty bars due to the temporal variation of ω . In this series, the value of h was fixed at $h = d = 1$. The main conclusion from these calculations is that the values of $\omega(k)$ follow the curve $\omega_h(k)$, where $\omega_h(k)$ is given by Eq. (26), but lie systematically some 20% below it. More specifically, for practical applications one can use a simple estimate

$$\omega(k) = (0.80 \pm 0.05) \omega_h(k), \tag{36}$$

for the linear growth rate of the RT instability in the case of direct shell acceleration with an initially uniform absorber–payload configuration. Equation (26) tells us that, when normalized to $(g/h)^{1/2}$, the values of ω_h depend on the product kh only. To verify how well this scaling is obeyed in practice, we have performed a single run with $h = 2$ and $k = 0.5$. The result, shown in Fig. 3 with an x cross, is indistinguishable from the corresponding case of $h = 1$ and $k = 1$. The effects of the fluid compressibility are relatively weak in our simulations: when the case of $\gamma = 2$, shown in Figs. 6 and 7(a), was recalculated with $\gamma = 5/3$, the range of ω variations shifted from $\omega = 0.77\text{--}0.93$ for $\gamma = 2$ to $\omega = 0.80\text{--}0.96$ for $\gamma = 5/3$ —in full agreement with Eq. (27).

V. IMPLICATIONS FOR THE NONLINEAR REGIME AND THE DMOT RATIOS

The calculated spectrum $\omega(k)$ of the linear growth rates allows us to make some general conclusions about possible enhancement of the distance-moved-over-thickness (DMOT) ratios. First of all note that the unperturbed solution of Sec. II represents the best (or close to the best) possible regime of shell acceleration for a given size h of the heating zone from the point of view of stabilization effects because it ensures a continuous density variation on a maximum possible scale h , which remains constant in space and time. To approach this regime in reality, one will generally need to do some pulse shaping. In practice, we are interested in situations when the ratio $h/d > 1$. For heavy ion pulses, typical realistic values should fall in the range $h/d \approx 2-10$.

First we assume that the external drive (ion beam heating) is perfectly uniform. Then, one can roughly distinguish between two qualitatively different patterns of shell rupture by the instability: (a) The shell breaks up when the exponential growth of initial perturbations with critical wave numbers $k_0 \approx d^{-1}$ begins to saturate at the end of the linear stage, or (b) the shell breaks up in the far nonlinear regime due to a self-similar growth of the mixing layer, $h_{\text{mix}}(t)$, which establishes itself at some small initial scale $h_{\text{mix}}(0) = k_0^{-1} \ll d$. Case (a) would correspond to situations with relatively large ($>1\% - 3\%$) initial perturbations (due, for example, to imperfections of target fabrication) on scales $k_0^{-1} \approx d$, whereas case (b) will be realized when the initial perturbations for all modes $k \leq d^{-1}$ are sufficiently small. In case (a), the distance travelled by an accelerated shell till its rupture, $s = \frac{1}{2} g t_{\text{rup}}^2$, is determined by a fixed number of e -foldings, $N_0 = \omega t_{\text{rup}}$, which, in its turn, is determined by the amplitude of the initial perturbations at $k \approx k_0 = d^{-1}$. Assuming the same level of initial perturbations, we evaluate the gradient-smoothed value of DMOT to be

$$\text{DMOT} = \frac{\omega_{\text{RT}}^2}{\omega^2} \text{DMOT}_{\text{RT}} \approx 1.5 \frac{h}{d} \text{DMOT}_{\text{RT}}, \quad (37)$$

where $\omega_{\text{RT}} = (gk_0)^{1/2} = (g/d)^{1/2}$ is the classical RT growth rate for $A = 1$, the value of $\omega = \omega(d^{-1})$ is given by Eq. (36), and $h > d$ is assumed. Thus, we calculate an enhancement factor of $1.5(h/d)$ for the distance travelled by the payload (hence, for its allowed in-flight aspect ratio) in the acceleration scheme of Fig. 1 as compared to the nonstabilized classical RT case of a strong density jump.

In case (b) the reference DMOT_{RT} ratio can be evaluated from Eq. (1) by assuming that the rupture time t_{rup} is measured from the moment when the self-similar regime (1) sets in on a scale $h_{\text{mix}}(0) = k_0^{-1}$,

$$\text{DMOT}_{\text{RT}} = \frac{1}{2\alpha_b} [1 - (k_0 d)^{-1/2}]^2. \quad (38)$$

In the limit of $k_0 d \gg 1$ the DMOT_{RT} ratio approaches its limiting value $(2\alpha_b)^{-1}$. The situation is qualitatively different for a continuous density variation with an exponential transition layer. In this case a self-similar mixing layer will advance into the payload exponentially in time,

$$h_{\text{mix}}(t) = k_0^{-1} \exp \left[\alpha_{bh} \left(\frac{g}{h} \right)^{1/2} t \right], \quad (39)$$

where the dimensionless constant α_{bh} —to the best of our knowledge—has not been calculated yet. Equation (39) can, for example, be easily deduced in the framework of the bubble competition model²² by noticing that $dh_{\text{mix}}/dt \sim u_b$, where $u_b \sim (2A_h g R_b)^{1/2} \sim (2A_h g h_{\text{mix}})^{1/2}$ is the saturated rise velocity of bubbles with the largest size $R_b \sim h_{\text{mix}}$, and the effective Atwood number A_h in the exponential atmosphere $\rho \sim \exp(y/h)$ “felt” by the mixing layer of thickness h_{mix} is $A_h = \tanh(h_{\text{mix}}/2h) \approx h_{\text{mix}}/2h$ for $h_{\text{mix}} < d < h$. The resulting distance-moved-over-thickness ratio,

$$\text{DMOT} = \frac{h \ln^2(k_0 d)}{d 2\alpha_{bh}^2}, \quad (40)$$

calculated from the condition $h_{\text{mix}}(t_{\text{rup}}) = d$, formally becomes infinitely large as the level of initial perturbations is reduced to zero, i.e., as $k_0 d \rightarrow \infty$. The latter means that (i) in contrast with the classical RT case of a density jump, the initial perturbations are always important in the gradient-stabilized case, and (ii) when the same initial perturbations are assumed for the classical and gradient-stabilized cases, the enhancement factor for achievable DMOT values, being $1.5(h/d)$ for $k_0 d = 1$, only increases as the initial perturbations are suppressed in amplitude and shifted to shorter characteristic wavelengths.

In what concerns the adverse effects of the drive nonuniformities, they are not necessarily linked to the RT instability. Even for stable configurations with zero initial perturbations, spatial variations of the heating rate in the x direction will generate corresponding fluctuations in the y -velocity of the payload. If, for example, such fluctuations are on a scale $k^{-1} \geq d$ and exceed 10% in amplitude, the payload shell will be strongly distorted after it travels a distance $s \geq 10d$ even when no instability occurs. In unstable situations, small perturbations introduced by the drive nonuniformities will, of course, be amplified by the instability. A detailed study should be performed in each particular case individually.

To give some feeling for a possible impact of a non-uniform heating, we have done several simulations for $g = 1$, $d = 1$, $h = 4$, $k = 1$ ($L = 2\pi$) with a perturbed heating rate

$$q(t, x, y) = [1 + a_{q0} \cos(kx)] \left[q_0(t) - \left(\frac{y}{h} \right)^2 q_1(t) \right], \quad (41)$$

where, as before, $q_0(t)$ and $q_1(t)$ are given by Eqs. (15) and (16). The initial fluid state was perfectly uniform along the x axis. When we start with a 10:1 density jump between regions III and I and set $a_{q0} = 0.1$, we observe a shell rupture at $t = t_{\text{rup}} = 7.4$, which corresponds to $\text{DMOT} \approx 27$. Since realistic DMOT values cannot exceed ≈ 10 because of the nonlinear mixing layer, we conclude that as high as 10% variations of the heating rate on a scale $k^{-1} \approx d$ can be tolerated in the classical RT case with a strong density jump. When we repeat this simulation with $a_{q0} = 0.1$ for a continuous density profile, we obtain practically the same rupture time $t_{\text{rup}} = 8$ and a similar DMOT value. A significant increase of the DMOT ratio beyond $1.5(h/d)$ $\text{DMOT}_{\text{RT}} \approx 60$, which corre-

sponds to $t_{\text{rup}} > 11$, has been obtained only after we decreased the perturbation amplitude below $a_{q0} \leq 0.01$.

VI. CONCLUSION

In the absence of the ablative stabilization, it is the stabilization by density gradient which becomes the principal mechanism of alleviating the Rayleigh–Taylor instability of thin shells accelerated by direct heating with intense ion beams. To verify that the heat conduction does not play any significant role, one can evaluate the corresponding time scale,

$$t_{ec} = \frac{c_V}{\kappa k^2}, \quad (42)$$

for smoothing of a sinusoidal temperature perturbation $\Delta T \propto \sin(kx)$; here c_V is the heat capacity per unit volume, and κ is the heat conduction coefficient. Taking gold at $\rho = 10 \text{ g/cm}^3$ and $T = 100 \text{ eV}$ (approximately an upper limit to the temperature in a heavy-metal absorber for realistic beam deposition rates) as an example, one obtains $t_{ec} \approx 10^{-7} \text{ s}$ for $L = 2\pi/k = 100 \text{ }\mu\text{m}$. This value of t_{ec} is still much larger than the RT time scale $t_{\text{RT}} = (gk)^{-1/2} \approx 1.3 \times 10^{-9} \text{ s}$, which one calculates for a typical acceleration of $g \approx 10^{15} \text{ cm/s}^2$.

With the beam deposition region fixed in space, a maximum stabilization by the density gradient is expected when the spatial and temporal profiles of the specific energy deposition are adjusted such that an adverse density gradient develops only gradually and on a maximum possible scale length h of the effective half-thickness of the beam deposition layer—as illustrated by a model solution for the unperturbed motion in Sec. II. Our 2D hydrodynamic simulations, conducted against the background of the analytic solution from Sec. II, demonstrate that the linear growth rate of small perturbations, localized near the payload–absorber interface, is adequately described by the limiting formula (26) for exponential transition layers scaled down by some 20%. By combining these numerical results for the linear growth rate with a qualitative analysis of the nonlinear regime, we deduce an enhancement factor of $1.5(h/d)$ for the distance-moved-over-thickness ratio relative to the classical RT case of a density jump with the Atwood number $A = 1$. This means that in our statement of the problem the stability issues favor large values of the absorber-to-payload mass ratio—a conclusion which is exactly opposite to the one reached by Magelssen²³ for the normal beam incidence in heavy ion ICF targets. With quite realistic values of $h/d = 3\text{--}5$, one can count on the DMOT values that are no less

than in the best cases of ablative stabilization—provided, of course, that a sufficiently low nonuniformity level of the beam deposition is ensured.

ACKNOWLEDGMENTS

One of the authors (M.M.B.) is grateful to the staff of the Institut für Kernphysik at TU Darmstadt, to Professor D. H. H. Hoffmann, and to all members of his group at the Gesellschaft für Schwerionenforschung (Darmstadt) for providing an office space, friendly assistance and many stimulating discussions during his three-month stay at the Frankfurt University—TU Darmstadt.

- ¹J. D. Lindl, *Inertial Confinement Fusion* (Springer, New York, 1998).
- ²D. A. Callahan-Miller and M. Tabak, *Phys. Plasmas* **7**, 2083 (2000).
- ³S. Bodner, *Phys. Rev. Lett.* **33**, 761 (1974).
- ⁴R. L. McCrory, L. Montierth, R. L. Morse, and C. P. Verdon, *Phys. Rev. Lett.* **46**, 336 (1981).
- ⁵H. Takabe, K. Mima, L. Montierth, and R. L. Morse, *Phys. Fluids* **28**, 3676 (1985).
- ⁶K. I. Read, *Physica D* **12**, 45 (1984).
- ⁷D. L. Youngs, *Physica D* **12**, 32 (1984).
- ⁸D. L. Youngs, *Phys. Fluids A* **3**, 1312 (1991).
- ⁹A. Caruso, V. A. Pais, and A. Parodi, *Laser Part. Beams* **10**, 447 (1992).
- ¹⁰D. H. H. Hoffmann, R. Bock, A. Ya. Faenov, U. Funk, M. Geissel, U. Neuner, T. A. Pikuz, F. Rosmej, M. Roth, W. Süß, N. Tahir, and A. Tauschwitz, *Nucl. Instrum. Methods Phys. Res. B* **161–163**, 9 (2000).
- ¹¹U. Neuner, R. Bock, C. Constantin, E. Dewald, U. N. Funk, M. Geissel, D. H. H. Hoffmann, J. Jacoby, A. Kozyreva, D. Penache, P. Pirzadeh, F. B. Rosmej, O. Rosmej, M. Roth, W. Süß, N. A. Tahir, A. Tauschwitz, S. Udrea, D. Varentsov, and H. Wahl, *Nucl. Instrum. Methods Phys. Res. A* **464**, 326 (2001).
- ¹²P. Spiller, J. Ahrens, K. Blasche, M. Emmerling, O. Boine-Frankenheim, B. Franczak, P. Hülsmann, G. Moritz, C. Mühle, W. Vinzenz, G. Walter, and P. Schütt, “A new high-intensity synchrotron SIS100 with strong bunch compression for GSI,” paper presented at the 2001 Particle Accelerator Conference, 18–22 June, 2001, Chicago.
- ¹³B. Yu. Sharkov, D. G. Koshkarev, M. D. Churazov, N. N. Alexeev, M. M. Basko, A. A. Golubev, and P. R. Zenkevich, *Nucl. Instrum. Methods Phys. Res. A* **415**, 20 (1998).
- ¹⁴N. A. Tahir, D. H. H. Hoffmann, A. Kozyreva, A. Shutov, J. A. Maruhn, U. Neuner, A. Tauschwitz, P. Spiller, and R. Bock, *Phys. Rev. E* **62**, 1224 (2000).
- ¹⁵M. M. Basko, *Phys. Plasmas* **7**, 4579 (2000).
- ¹⁶S. Chandrasekhar, *Hydrodynamic and Hydromagnetic Stability* (Clarendon, Oxford, 1961).
- ¹⁷H. J. Kull, *Phys. Rep.* **206**, 199 (1991).
- ¹⁸K. O. Mikaelian, *Phys. Rev. A* **26**, 2140 (1982).
- ¹⁹V. N. Goncharov, P. McKenty, S. Skupsky, R. Betti, R. L. McCrory, and C. Cherfils-Clérouin, *Phys. Plasmas* **7**, 5118 (2000).
- ²⁰R. Bandiera, *Astron. Astrophys.* **139**, 368 (1984).
- ²¹F. L. Addessio, J. R. Baumgardner, J. K. Dukowicz, N. L. Johnson, B. A. Kashiwa, R. M. Rauenzahn, and C. Zemach, “CAVEAT: A Computer Code for Fluid Dynamics Problems With Large Distortion and Internal Slip,” LA-10613-MS, Rev. 1, UC-905 (Los Alamos, 1992).
- ²²U. Alon, J. Hecht, D. Ofer, and D. Shvarts, *Phys. Rev. Lett.* **74**, 534 (1995).
- ²³G. R. Magelssen, *Nucl. Fusion* **24**, 1527 (1984).